Electronic Supplementary Material (ESI) for Nanoscale.

Supporting Information

$MnPS_3$ Spin-Flop Transition-Induced Anomalous Hall Effect in Graphite Flake via van der Waals Proximity Coupling

Ying Zhang[1#], Wenhui Wang[2#], Meng Huang[1], Ping Liu[1], Guojing Hu[1], Chao Feng[1], Xueyan Lei[1], Meng Gu[3], Hongxin, Yang[4], Kaihui Liu[5], Bin Xiang[1]*, Yalin Lu[1]

Supplementary Information Text

Note S1. Two components of anomalous Hall effect separation

The detail method for separating the positive and negative anomalous Hall effect (AHE) components has been introduced in the reported literatures.[1] In this method, we consider that the negative component has a rather lower saturation field than the positive component AHE ($B_{n,s}$ <$B_{p,s}$). Thus the positive component is responsible for the variation of the total AHE resistivity in the field range from $B_{n,s}$ to $B_{p,s}$. As demonstrated in the figure 1d (black line), the total AHE resistivity is perfectly fitted by a linear relationship in the field of B_n < 0.2 T< B < 0.4 T < B_p, and the $k = d\rho_{AHE}/dB$ is used as the slop of the positive component AHE for the fields |B|<0.4 T. After determining the positive component AHE resistivity at lower field, the negative component AHE resistivity can be obtained by the following equation: $\rho_{AHE,\ N}(B) = \rho_{AHE}(B) - kB$, where the ρ_{AHE} (B) is the total AHE resistivity for the total range of fields. The average value of $\rho_{AHE,\ N}$ (B) for the approximate field of 0.2<B<0.4 T is used as the saturated negative component AHE resistivity at higher field, and finally the complete $\rho_{AHE,\ P}$ (B) is obtained by subtracting the $\rho_{AHE,\ N}$ (B) from the ρ_{AHE} (B) for the full range of magnetic field.

The decomposition of the total AHE into positive and negative component AHE is a kind of ambiguousness in the point of view of math, for example, the linear part at low magnetic field range is ambiguous. However, the turning point A in total AHE and B in component AHE are in a one-to-one correspondence as shown in Figure S8, and the saturation field of AHE is also determined precisely. More importantly, the total AHE in graphite flake is composed of two AHE contributions of different mechanisms. One AHE (positive component) is induced by the nonzero perpendicular

magnetic moment of $MnPS_3$. The other AHE (negative component) is due to the enhanced spin-orbital coupling scattering at the interface of $MnPS_3$/graphite flake. Therefore, it makes sense for us to decompose the total AHE into two parts of AHE which is also controllable at certain point.

Note S2. The mechanisms of the anomalous Hall effect

The mechanism of the anomalous Hall effect has been usually classified into extrinsic and intrinsic origin. The extrinsic origin includes skew scattering and side jump mechanisms that are proposed by Smit and Berger,[2] respectively. The skew scattering mechanism suggests that the spin polarized electrons are scattered to one side by spin-orbit coupling due to the existing of impurities, which gives a relation of $\rho_{AH} \sim \rho_{xx}$. The side jump mechanism is closely related to the process of scattering event with impurity ions, which shows $\rho_{AH} \sim \rho^2_{xx}$. These extrinsic mechanisms are based on the complicated contribution of impurities and spin-orbit coupling which are different from the intrinsic mechanism, the latter is dependent on the Berry curvature in the materials. Interestingly, the anomalous Hall resistivity dominated by Berry curvature is also quadratic proportionality to the longitudinal resistivity ($\rho_{AH} \sim \rho^2_{xx}$), which shows similar relation to that of side jump mechanism. But the side jump contribution is negligibly small compared to Berry curvature contribution.[3]

Note S3. The mechanisms of the *negative-component* AHE

As shown in Figure S4, the fitting curve for the experimental data of ρ_{AHE} vs. ρ_{xx} indicates that the relation ρ_{AHE} vs. ρ_{xx} can be described by $\rho_{AHE}=E\rho_{xx}$ at temperatures higher than 90 K. This fitting result suggests that only an extrinsic mechanism of skew scattering dominates the high-temperature negative-component AHE. In our $MnPS_3$/GF device, the nonzero perpendicular component of the $MnPS_3$ magnetic moment induces ferromagnetic ordering in GF through the magnetic proximity

effect.[4] Therefore, those magnetizations as the center cause the scattering events and have a contribution to the negative-component AHE of GF. The negative-component AHE can persist up to room temperature. We attribute this high temperature phenomena to spin-momentum locking in GF surface.[5] The electron spins can be locked to the momentum due to the enhanced SOC in the surface, which leads to the enhancement of the proximity-induced magnetic ordering temperature of GF.

Note S4. AFM properties of $MnPS_3$

We have measured the M-T and M-H data of bulk $MnPS_3$ as shown in Figure S3 and Figure S5 for verifying the AFM behavior of $MnPS_3$. The M-T curve of an out-of-plane antiferromagnetic behavior in $MnPS_3$, exhibits nearly zero magnetic moment at a very low temperature which is consistent with the reported results.[6-8] However, the M-H curve (Figure S5a) shows that an external magnetic field parallel to c-axis that is high enough to overcome the anisotropy field can lead to the spin-flop transition of the $MnPS_3$ magnetization and a nonzero perpendicular component magnetization as shown in Figure S5b. We believe that this nonzero perpendicular component of $MnPS_3$ magnetization induces the anomalous Hall effect in the adjacent graphite flake through a magnetic proximity effect.

Note S5. Theoretical calculations on $MnPS_3$/graphite flake

$MnPS_3$ is typical two-dimensional (2D) monoclinic structure, who belongs to the $C2/m$ space group with lattice parameters of $a = 6.077$ Å, b=10.524 Å, c=6.796 Å, and $\beta = 107.35°$. To study the magnetic ground states of the $MnPS_3$, we utilize the density functional theory (DFT) and apply the projector augmented wave (PAW)[9,10] method which is encoded in the Vienna ab initio simulation package (VASP).[11, 12] The exchange-correlation functional is subjected to the generalized gradient approximation (GGA) in the parametrization of Perdew, Burke, and Enzerh.[13]

Berry curvatures:

We study the $B_n(\vec{k})$ by the method of Wisloop to performance the flux in a numeral calculation's method:

$$B_n\left(\vec{k}\right)=\frac{1}{2\pi}\arg(\left\langle\varphi_{n,1}^{R}\middle|\varphi_{n,2}^{R}\right\rangle\left\langle\varphi_{n,2}^{R}\middle|\varphi_{n,3}^{R}\right\rangle\left\langle\varphi_{n,3}^{R}\middle|\varphi_{n,4}^{R}\right\rangle\left\langle\varphi_{n,4}^{R}\middle|\varphi_{n,1}^{R}\right\rangle)$$

Where the subscripts 1 to 4 denote the eigen states on a square infinitesimally close to $\vec{k}$.

Note S6. The device surface characterization

The $MnPS_3$ and graphite are layered structural materials with van der Waals interlayer interaction. Therefore, it is easy for us to achieve a flat surface by a mechanical exfoliation method. We have characterized the surface of $MnPS_3$/graphite flake using atomic force microscopy (AFM) as shown in Figure S9(a). The AFM image shows smooth surface without any atomic-layer-thick step on either $MnPS_3$ or graphite flake surface. We have also characterized the cross-section of the $MnPS_3$/graphite flake device by utilizing focus ion beam (FIB) technique as shown in Figure S9(b). We didn't observe any kink or bubble features in the cross-section image. Therefore, we believe that our device surface is free of roughness.

Note S7. The definition of transition temperature

We define the transition temperature by plotting the tangent line on the AHE resistivity vs. Temperature curves as shown in Figure S2. The temperature dependence of the anomalous Hall resistivity is determined by the temperature dependence of the magnetization because of spin-orbital coupling.[14] Therefore, a sudden change in the slope of Figure S2. can be utilized to demonstrate the change of magnetic order. The $\rho_{AHE,\,P}$ exhibits a slight increase when the temperature is cooled from room temperature. As the temperature reaches 73 K, the $\rho_{AHE,\,P}$ shows a rapid increase. This temperature is close to the $MnPS_3$ Néel temperature of 78 K. When we apply an external magnetic

field perpendicular to the surface of the device at a temperature below 73 K, a spin-flop effect of $MnPS_3$ occurs, which induces the AHE effect by a proximity coupling. Therefore, from the evolution of the $\rho_{AHE,\,P}$ as a function of temperature, we treat the obtained temperature of 73 K as a transition temperature for positive AHE. Regarding the negative AHE, the temperature of 100 K is treated as a critical temperature with different mechanism contributions, which mechanisms are still needed to be further studied in the future.

Note S8. Exclusion from multi-carrier mechanism

The Fermi level of intrinsic GF can be adjusted by the back-gate voltage, which means that the GF can change the carrier type between hole and electron. If the nonlinear Hall effect behavior is dominated by multi-carrier mechanism, the Hall resistivity would change its signs during our gate-voltage scanning, because the gating voltage is much larger than the neutral point of GF. In our $MnPS_3$/GF device, the sign of AHE derived from nonlinear Hall resistivity is unchanged which eliminates the multi-carrier mechanism and confirms that the nonlinear results from the spin electron.[15]

Note S10. Device performance at different thickness

We carried out the measurement of the GF thickness dependence of AHE as shown in Figure S10. All the thickness of $MnPS_3$ are maintaining in ~ 14 nm. The Figure S10 shows that a larger thickness of GF exhibits higher AHE saturation resistivity The reason is that the relation ρ_{AHE} vs. ρ_{xx} can be described by $\rho_{AHE}=C\rho_{xx}+D\rho_{xx}^2$ in the temperature range of 3-90 K, revealing that both the intrinsic mechanism of Berry curvature and extrinsic mechanism of skew scattering dominate the low-temperature AHE. The thickness increase in the GF can cause a shift of the Fermi level E_F towards

the Dirac point,[16] which can induce a decrease in the carrier concentration of GF. As a result, the resistivity of GF ρ_{xx} is increased when the layer thickness increases. Therefore, the AHE resistivity ρ_{AHE} is increased in the thicker graphite flake as shown in Figure S10.

Figures

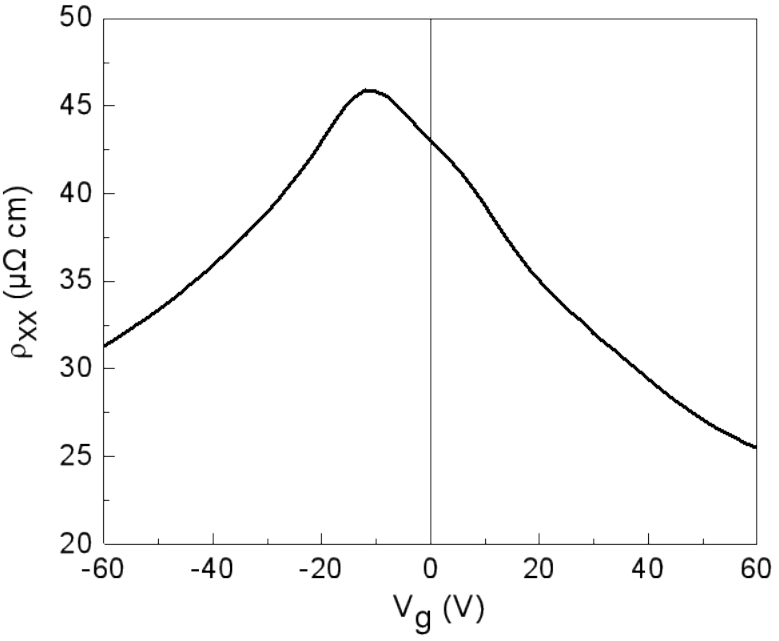

Figure S1. Gate-voltage tuning longitudinal resistivity. The gate voltage dependence of the longitudinal resistivity data under 3 K and 1.4 T, where the neutral point is -10 V.

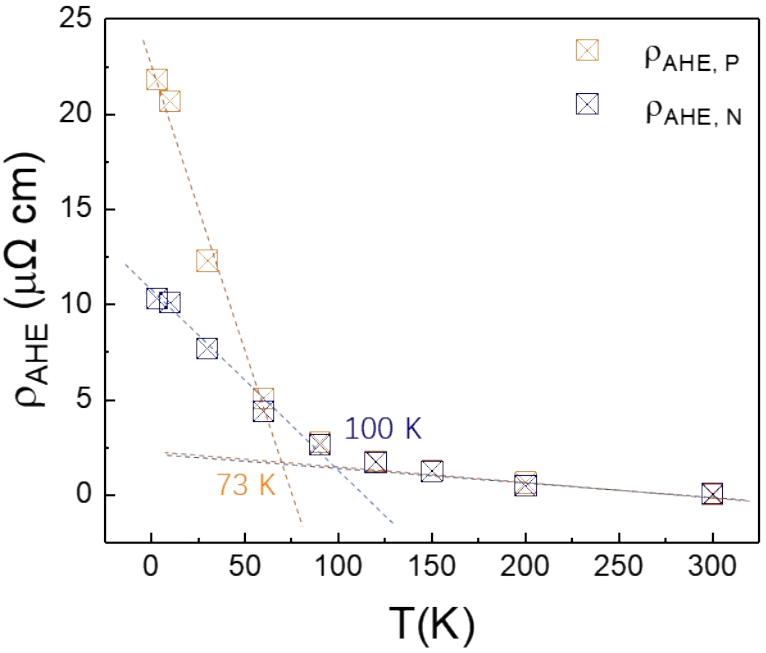

Figure S2. Characteristics of the AHE resistivity. The positive and *negative-component* AHE resistivity as a function of the temperature at 1 T.

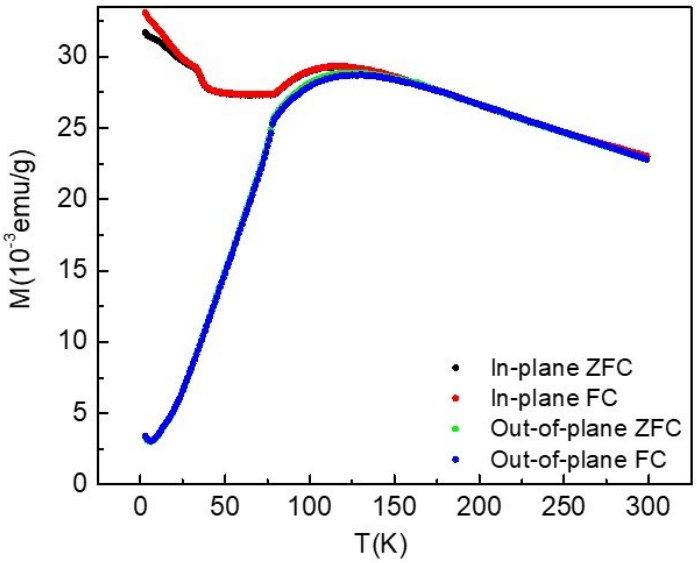

Figure S3. M-T curve of the $MnPS_3$. The temperature dependence of the $MnPS_3$ magnetization for applying in-plane and out-of-plane magnetic field with zero field cooling (ZFC) and field cooling (FC) processes.

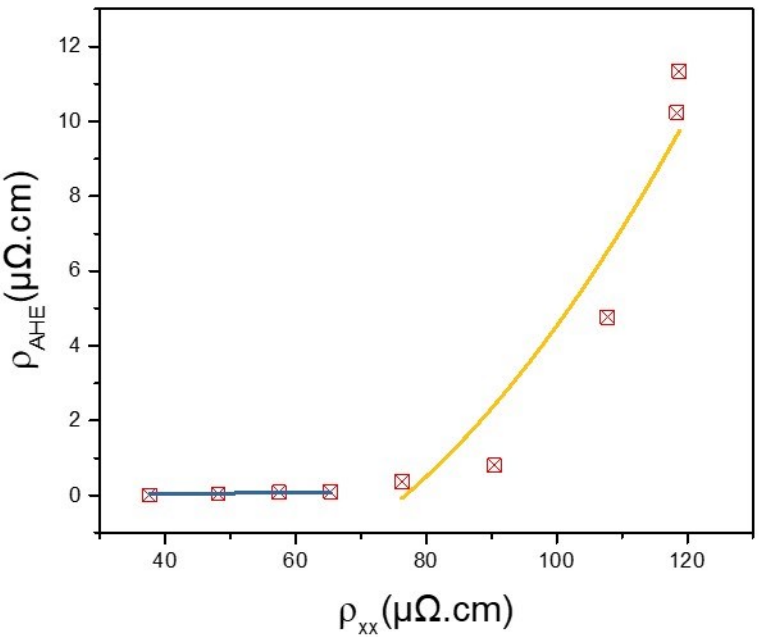

Figure S4. Fitting of the AHE resistivity. The AHE resistivity as a function of the longitudinal resistivity at 1.4 T at different temperature (red dot) and the corresponding fitting curves at low temperature (yellow) and high temperature (navy), respectively.

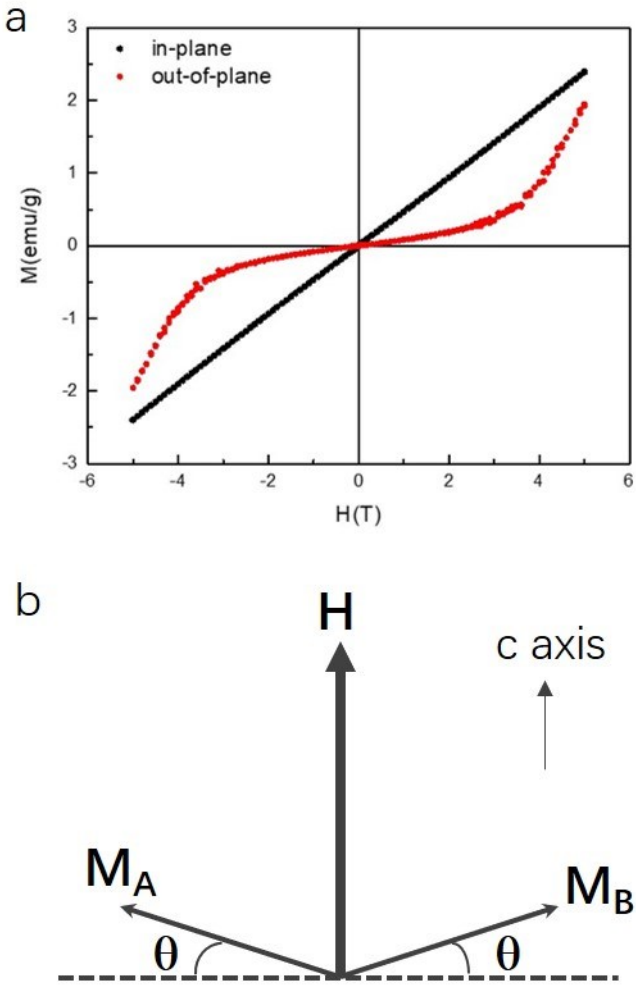

Figure S5. M-H data of $MnPS_3$. (a) The magnetizing curve of $MnPS_3$ for applying in-plane (black dot) and out-of-plane (red dot) magnetic field, respectively, at 10 K. **(b)** The illustration spin-flop transition of $MnPS_3$ magnetization with nonzero perpendicular component of magnetic moment when external magnetic field (H) is applied along c axis.

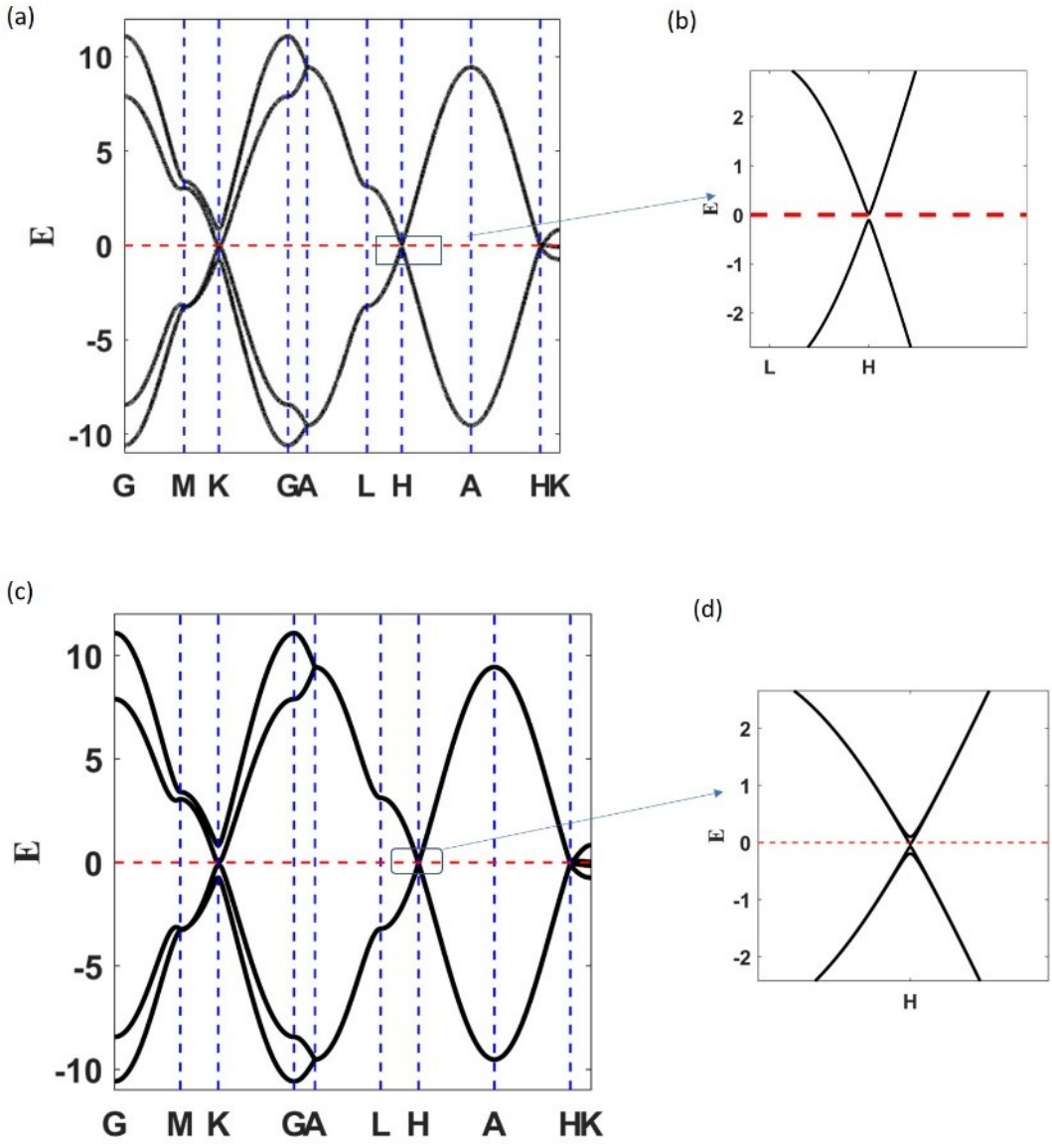

Figure S6. Band structures of graphite flake (a) Band structure of graphite flake without SOC. (b) Zoom in (a) at H point. (c) Band structure of graphite flake with SOC. (d) Zoom in (c) at H point.

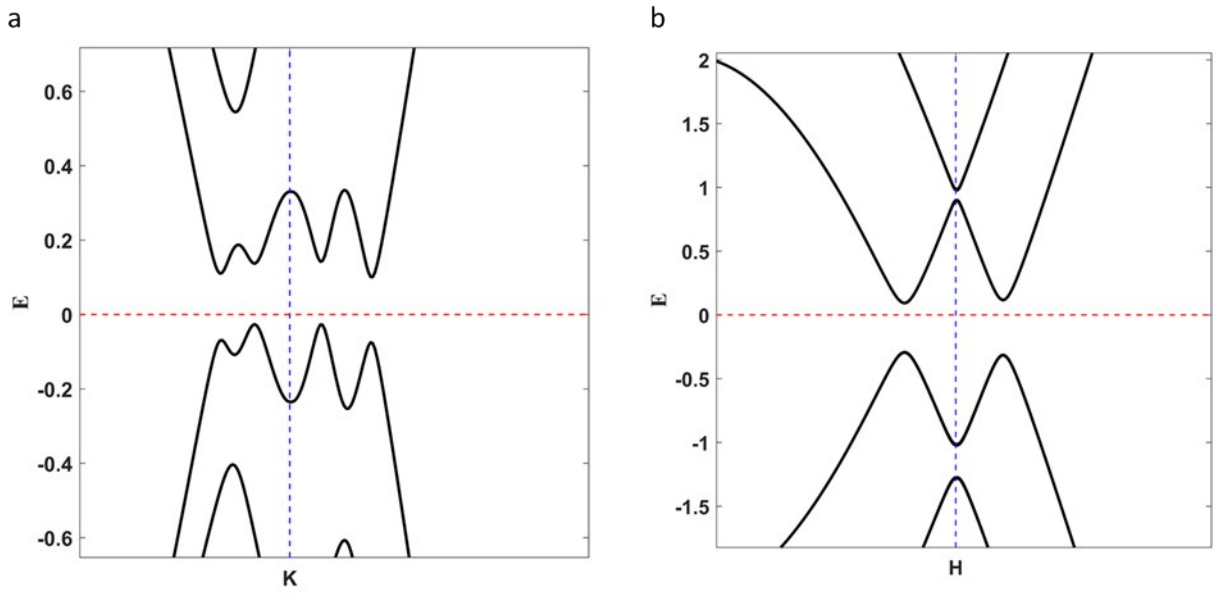

Figure S7. Band structure of bulk graphite with SOC and out-plane Zeeman field (a) around K point (b) around H point.

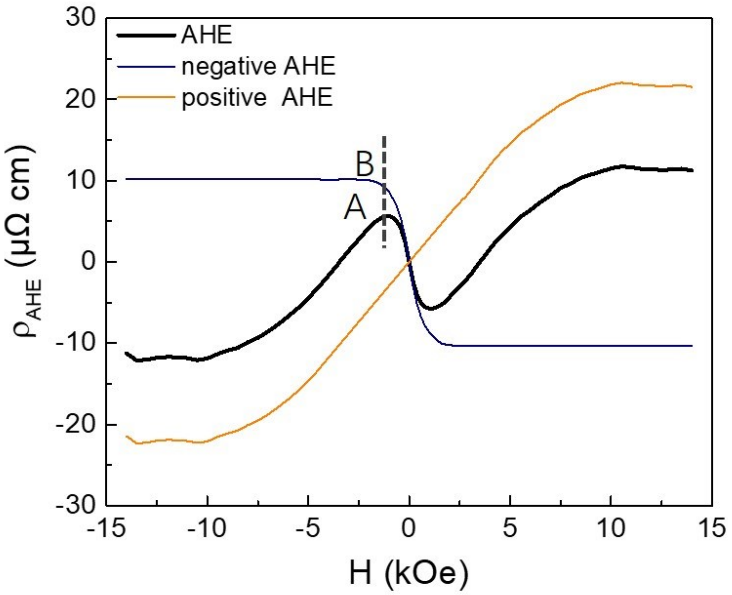

Figure S8. Magnetic field dependence of the total AHE resistivity (black), *negative-component* AHE resistivity (navy) and *positive-component* AHE resistivity (dark yellow) at 3 K.

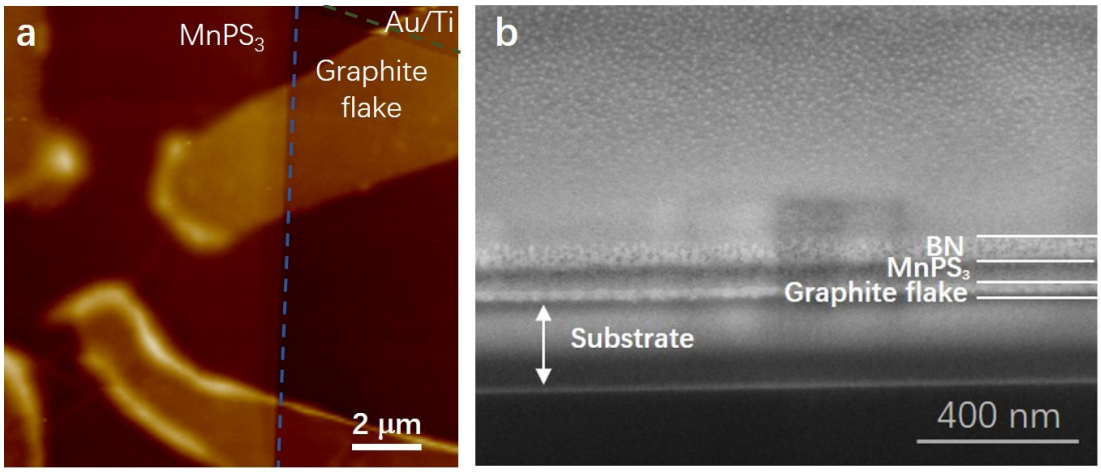

Figure S9. Microscope picture of device. (a) AFM image of the $MnPS_3$/Graphite flake device. (b) The SEM image of the cross-section of the $MnPS_3$/Graphite flake device.

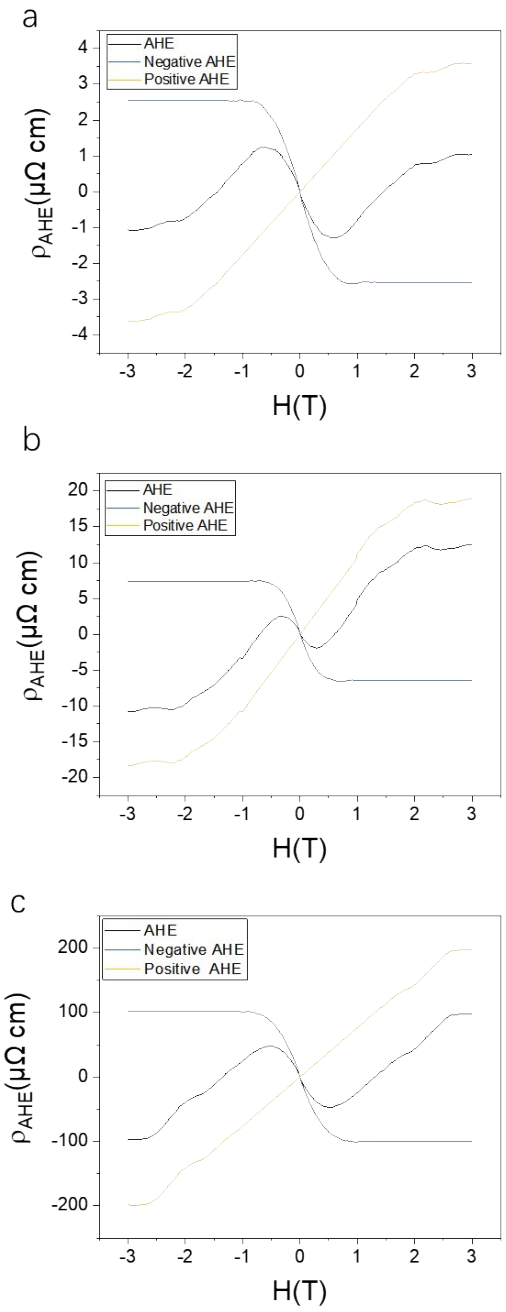

Figure S10. Magnetic field dependence of the total AHE resistivity (red), negative-component AHE resistivity (navy) and positive-component AHE (dark yellow) with different thickness of graphite at 3 K. (a) The 4 nm-thick graphite flake. (b) The 6 nm-thick graphite flake. (c) the 13 nm-thick graphite flake. All of the thickness of the $MnPS_3$ are ~ 14 nm.

References:

1 N. Liu, J. Teng and Y. Li, Two-component anomalous Hall effect in a magnetically doped topological insulator, *Nat. Comm.,* 2018, **9,** 1282.

2 N. Nagaosa, J. Sinova, S. Onoda, A. H. MacDonald and N. P. Ong, Anomalous Hall effect, *Rev. Mod. Phys.,* 2010, **82,** 1539-1592.

3 T. Miyasato, N. Abe, T. Fujii, A. Asamitsu, S. Onoda, Y. Onose, N. Nagaosa and Y. Tokura, Crossover behavior of the anomalous Hall effect and anomalous nernst effect in itinerant ferromagnets, *Phys. Rev. Lett.,* 2007, **9,** 086602.

4 S. LaShell, B. A. McDougall and E. Jensen, Spin splitting of an Au(111) surface state band observed with angle resolved photoelectron spectroscopy, *Phys. Rev. Lett.,* 1996, **77,** 3419.

5 F. Katmis, V. Lauter, F. S. Nogueira, B. A. Assaf, M. E. Jamer, P. Wei, B. Satpati, J. W. Freeland, I. Eremin, D. Heiman, P. Jarillo-Herrero and J. S. Moodera, A high-temperature ferromagnetic topological insulating phase by proximity coupling, *Nature,* 2016, **533,** 513–516.

6 Y. Shiomi, R. Takashima and E. Saitoh, Experimental evidence consistent with a magnon Nernst effect in the antiferromagnetic insulator $MnPS_3$, *Phys. Rev. B,* 2017, **96,** 134425.

7 G. Long, O. Zhang, X. Cai, J. Hu, C. Cho, S. Xu, J. Shen, Z. Wu, T. Han, J. Lin, J. Wang, Y. Cai, R. Lortz, Z. Mao and N. Wang, Isolation and characterization of few-layer manganese thiophosphate, *ACS Nano,* 2017, **11,** 11330-11336.

8 K. Okuda, K. Kurosawa, S. Saito, M. Honda, Z. Yu and M. Date, Magnetic properties of layered compound $MnPS_3$, *J. Phys. Soc. Jpn.,* 1986, **55,** 4456-4463.

9 J. P. Perdew, K. Burke and M. Ernzerhof, Generalized gradient approximation made simple, *Ph*ys. *Rev. Lett.,* 1996, **77,** 3865-3868.

10 G. Kresse and D. Joubert, From ultrasoft pseudopotentials to the projector augmented-wave method, *Phys. Rev. B,* 1999, **59,** 1758-1775.

11 G. Kresse and J. Furthmüller, Efficient iterative schemes for ab initio total-energy calculations using a plane-wave basis set, *Phys. Rev. B,* 1996, **54,** 11169.

12 J. Hafner, Ab-Initio simulations of materials using VASP: density-functional theory and beyond,

J. Comput. Chem., 2008, **29,** 2044-2078.

13 P. E. Blo¨chl, Projector augmented wave method:ab initiomolecular dynamics with full wave functions, Phys. *Rev. B: Condens. Matter Mater. Phys.,* 1994, **50,** 17953-17979.

14. G. Bergmann, F. Ye, Absence of a low-temperature anomaly of the anomalous Hall conductivity in thin amorphous ferromagnetic Fe films, *Phys. Rev. Lett.,* 1991, **67,** 735.

15. K. Gopinadhan, Y. J. Shin, R. Jalil, T. Venkatesan, A. K. Geim, A. H. Castro Neto, H. Yang, Extremely large magnetoresistance in few-layer graphene/boron–nitride heterostructures, *Nat. Commun.,* 2015, **6,** 8337.

16. R. Wang, S. Wang, D. Zhang, Z. Li, Y. Fang, X. Qiu, Control of carrier type and density in exfoliated graphene by interface engineering, *ACS Nano,* 2010, 5, 408-412.